



# Dwarf Satellites of High- $z$ Lyman Break Galaxies: A Free Lunch for JWST

Viola Gelli<sup>1,2</sup> , Stefania Salvadori<sup>1,2</sup> , Andrea Ferrara<sup>3</sup> , Andrea Pallottini<sup>3</sup> , and Stefano Carniani<sup>3</sup>

<sup>1</sup> Dipartimento di Fisica e Astronomia, Università degli Studi di Firenze, via G. Sansone 1, I-50019, Sesto Fiorentino, Italy; [viola.gelli@unifi.it](mailto:viola.gelli@unifi.it)

<sup>2</sup> INAF/Osservatorio Astrofisico di Arcetri, Largo E. Fermi 5, I-50125, Firenze, Italy

<sup>3</sup> Scuola Normale Superiore, Piazza dei Cavalieri 7, I-56126 Pisa, Italy

Received 2021 March 12; revised 2021 May 6; accepted 2021 May 6; published 2021 May 31

## Abstract

We show that the James Webb Space Telescope (JWST) will be able to detect dwarf satellites of high- $z$  Lyman break galaxies (LBGs). To this end, we use cosmological simulations following the evolution of a typical  $M_* \simeq 10^{10} M_\odot$  LBG up to  $z \simeq 6$ , and analyze the observational properties of its five satellite dwarf galaxies ( $10^7 M_\odot < M_* < 10^9 M_\odot$ ). Modeling their stellar emission and dust attenuation, we reconstruct their rest-frame ultraviolet-optical spectra for  $6 < z < 6.5$ . JWST/NIRCam synthetic images show that the satellites can be spatially resolved from their host, and their emission is detectable by planned deep surveys. Moreover, we build synthetic spectral energy distributions and color-magnitude diagrams for the satellites. We conclude that the color F200W–F356W is a powerful diagnostic tool for understanding their physical properties once they have been identified. For example,  $F200W-F356W \lesssim -0.25$  can be used to identify star-bursting ( $SFR \sim 5 M_\odot \text{ yr}^{-1}$ ), low-mass ( $M_* \lesssim 5 \times 10^8 M_\odot$ ) systems, with  $\sim 80\%$  of their stars being young and metal poor [ $\log(Z_*/Z_\odot) < -0.5$ ].

*Unified Astronomy Thesaurus concepts:* [High-redshift galaxies \(734\)](#); [Dwarf galaxies \(416\)](#); [Cosmology \(343\)](#)

## 1. Introduction

The James Webb Space Telescope (JWST; Gardner et al. 2006) will provide unprecedented observations of the most distant galaxies, revolutionizing our knowledge of the high-redshift Universe. It will be able to detect remarkably faint objects during the Epoch of Reionization (EoR;  $z \gtrsim 6$ ) reaching ultraviolet (UV) absolute magnitudes of  $M_{UV} \simeq -15$  at redshift  $z \simeq 6$  (e.g., Finkelstein 2016). The wavelength coverage of instruments like NIRCam (0.6–5  $\mu\text{m}$ , Horner & Rieke 2004) will allow us to study their rest-frame optical and UV properties for the first time.

Among the faint objects expected to be present in large numbers at high- $z$  are dwarf galaxies ( $M_* \lesssim 10^9 M_\odot$ ). Indeed, according to the hierarchical  $\Lambda$ CDM model, dwarf galaxies are the most abundant systems at all cosmic times, being the first galaxies to form and the basic building blocks of the massive galaxies that we see today.

The physical and observational properties of *isolated* dwarf galaxies located in the field have been widely studied through cosmological simulations (Wise et al. 2014; Zackrisson et al. 2017; Jeon & Bromm 2019). However, we also expect the presence of an additional category of dwarf galaxies: the *satellites* orbiting around more massive galaxies in the densest regions of the cosmic web (e.g., Conroy et al. 2006). In particular, Gelli et al. (2020) showed that a typical massive  $z \simeq 6$  Lyman break galaxy (LBG) is surrounded by dwarf satellites, living inside its virial halo. These satellites represent an interesting complementary population with respect to isolated field dwarf galaxies, since their properties and evolution are affected by the peculiar environment in which they dwell.

JWST is expected to detect many LBGs: the emission of dozens of them will most likely appear already within the deep fields of high-priority surveys like the JWST Advanced Deep Extragalactic Survey (JADES; Rieke et al. 2019), that will reach exposure times of  $\sim 20$  hr for imaging with NIRCam. This provides the remarkable opportunity to exploit planned

JWST surveys to detect *for the first time and for free* their dwarf satellite population.

Will JWST be able to effectively detect dwarf satellites of massive LBGs through imaging and photometry? Will such observations shed light on the star formation rates, stellar metallicity, and presence of young/metal-poor stars in these systems? We address these issues by using high-resolution, zoom-in cosmological simulations (Pallottini et al. 2017) reproducing the evolution of a typical  $z \simeq 6$  LBG. In Gelli et al. (2020) we studied the stellar populations of the dwarf satellites. Here, we make a further step and model their emission, focusing on the stellar continuum.

## 2. Method

### 2.1. Simulating High- $z$ LBGs and Their Dwarf Satellites

To study the emission of LBGs dwarf satellites at high- $z$ , we use a high-resolution ( $\lesssim 30$  pc) zoom-in cosmological simulation, fully described in Pallottini et al. (2017). It adopts a customized version of the adaptive mesh refinement code RAMSES (Teyssier 2002) to follow the evolution of a prototypical LBG called Althæa. Stellar particles in the simulation form according to an  $H_2$  dependent Schmidt–Kennicutt relation (Kennicutt 1998), where the abundance of molecular hydrogen is computed by a non-equilibrium chemical network via the KROME code (Grassi et al. 2014). Stellar evolution is modeled accounting for energy inputs and yields by using STARBURST99 (Leitherer et al. 1999), assuming PADOVA (Bertelli et al. 1994) stellar tracks and a Kroupa initial mass function (Kroupa 2001). Since the simulation cannot follow the formation of the first stars in pristine mini-halos, a metallicity floor of  $Z_{\text{floor}} = 10^{-3} Z_\odot$  has been imposed to mimic the consequences of the first stellar generations on metal enrichment (Wise et al. 2012; Pallottini et al. 2014).

At  $z \sim 6$  the simulated LBG Althæa has a stellar mass of  $M_* \sim 10^{10} M_\odot$  and a star formation rate ( $SFR$ )  $\sim 50 M_\odot \text{ yr}^{-1}$ .

The target halo hosts five dwarf satellites and one proto-globular cluster orbiting around the central massive LBG

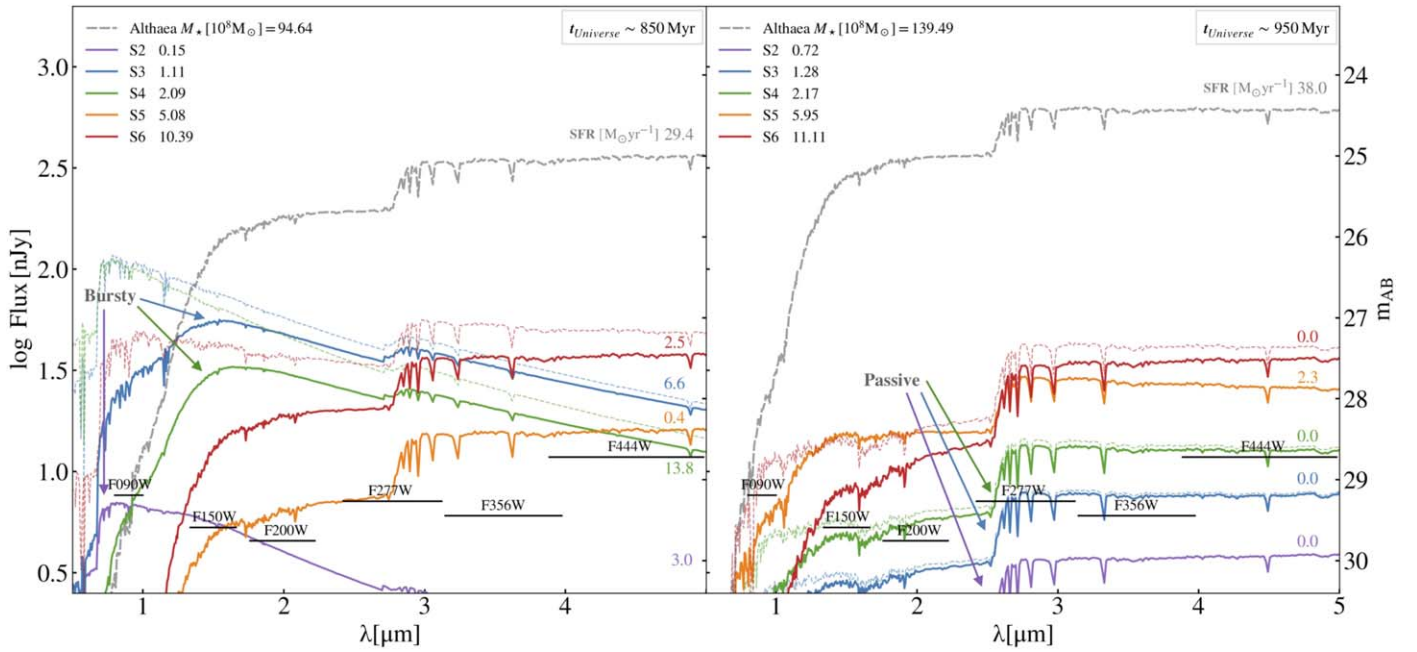


**Figure 1.** SEDs for the five high- $z$  satellites (colored continuous curves) and the central LBG Althaea (gray dashed) shown at two different times. Left panel: bursty phase ( $z \approx 6.5$ ), in which the three smallest satellites are experiencing a star formation burst. Right panel: passive phase about 100 Myr later ( $z \approx 6$ ), when star formation has been quenched. The black horizontal lines show the sensitivities of JWST/NIRCam filters for point sources with signal-to-noise ratio (S/N) = 5 and exposure time of  $\sim 3$  hr. The dashed curves show the intrinsic (i.e., unattenuated) stellar emission for three satellites.

( $r < 10$  kpc); their stellar properties are thoroughly analyzed in Gelli et al. (2020). The satellites can be divided into two main groups based on their mass, differing in terms of both evolutionary and chemical properties. Low-mass systems ( $M_* \lesssim 5 \times 10^8 M_\odot$ ) form their stellar populations in short bursts ( $\sim 50$  Myr), after which star formation is completely suppressed by supernova (SN) feedback. More massive satellites are characterized instead by long and complex star formation histories (SFHs; see Figures 7 and 8 of Gelli et al. 2020), resulting from the balance between feedback and merger events bringing new gas to fuel star formation.

Perhaps surprisingly, at  $z \sim 6.5$  the interstellar medium (ISM) of all the satellites is already enriched in heavy elements ( $Z_{\text{ISM}} \geq 10^{-2} Z_\odot$ ), and most likely in dust. These high metallicities are due to: (i) pre-enrichment of the environment by the central LBG and its progenitors, for the case of low-mass satellites; (ii) in situ star formation for massive satellites, which form their first stellar generations at  $z > 9$  in a nearly pristine environment (Gelli et al. 2020). In spite of their low initial metallicities, high-mass satellites contain a smaller fraction of metal-poor (defined as  $[\log(Z_*/Z_\odot) < -0.5]$ ) stars ( $\lesssim 20\%$ ) with respect to smaller systems ( $\gtrsim 50\%$ ) because of their longer SFHs.

## 2.2. Spectral Energy Distribution (SED) Building and Synthetic Images

To derive the intrinsic SEDs of the dwarf satellites based on their simulated stellar populations, we use STARBURST99 (Leitherer et al. 1999), also consistent with the simulation prescriptions. We proceed as follows: considering the total SFH of the selected galaxy (up to  $z \sim 6$ , final snapshot of the simulation), we sample it in timesteps of  $\Delta t = 5$  Myr, which assure a good convergence for the spectra. At each timestep we consider a single burst of star formation: the stellar mass,

metallicity, and formation time are given as an input to STARBURST99. The final output consists in the rest-frame intrinsic spectrum of the galaxy at all times from its formation up to  $z \sim 6$ .

The intrinsic spectrum can be attenuated by dust, for which we adopt the SMC synthetic extinction curve by Weingartner & Draine (2001). This is the natural choice for dwarf galaxies and a good approximation for high- $z$  sources at  $\lambda > 0.3 \mu\text{m}$  (Gallerani et al. 2010). We compute the optical depth as:  $\tau = C_{\text{ext}} \times N_{\text{H}} [\text{cm}^{-2}] \times Z [Z_\odot]$ , where  $C_{\text{ext}}$  is the tabulated cross section per H nucleon, and  $N_{\text{H}}$  and  $Z$  are the gas hydrogen column density and metallicity averaged on different line of sights. The latter two are retrieved directly from the simulation, considering the gas composition in the selected satellite galaxy at the snapshots available (i.e., every 18 Myr), and interpolating at intermediate times. The final SEDs (Figure 1) are obtained by reprocessing the intrinsic stellar spectra with the derived dust transmission curves.

To enable a detailed spatial/morphological analysis, we have produced synthetic images of the central LBG and its dwarf satellites at  $z \sim 6$  (Figure 2). The images are built from stellar density maps of the simulated, face-on LBG disk (e.g., see Figure 2 in Gelli et al. 2020), and using the proportionality between stellar mass and observed magnitude in the selected bands. We simulate the instrument effects by convolving the high-resolution images with a Gaussian with the FWHM of the selected NIRCam filter, and then rebinning to match the instrument pixel size. No sky background has been simulated when creating the images.

## 3. Results

The resulting SEDs of the satellites and the central LBG Althaea are shown in Figure 1, in the NIRCam wavelength range,  $0.6\text{--}5 \mu\text{m}$ , and for two different redshifts:  $z \approx 6.5$  (left

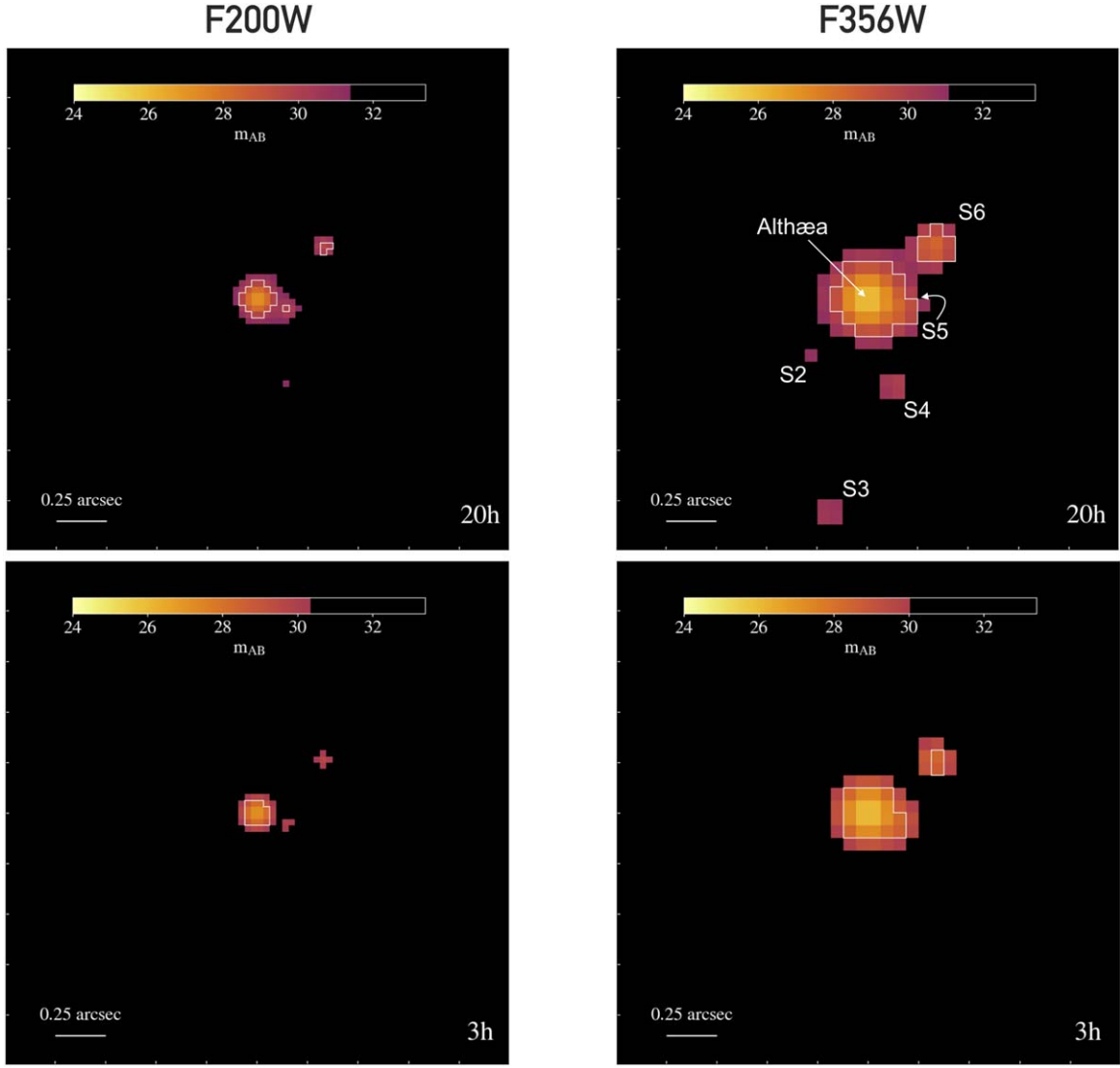


**Figure 2.** Synthetic images centered on the LBG at  $z = 6$  in a field of view of size  $2''.5 \times 2''.5$ , corresponding to  $15 \times 15$  kpc. The maps are displayed in two NIRC filters: F200W (left column, short-wavelength channel with pixel scale of  $0''.032$ ) and F356W (right column, long-wavelength channel with pixel scale of  $0''.065$ ), and for exposure times of 20 hr (top row) and 3 hr (bottom row). The images are shown for  $S/N = 3$  and the white contours identify the pixels with  $S/N = 10$ . The location of the satellites are pinpointed by the labels S2,...,S6 from the least to the most massive system.

panel) and  $z \simeq 6$  (right panel). We adopt the same notation as in Gelli et al. (2020) to indicate the satellites, i.e., they are named from S1 to S6 with increasing stellar mass. S1 is the proto-globular cluster: its flux is more than 2 orders of magnitude below that of the other satellites, hence invisible even for JWST deep surveys. We notice that the flux of the central LBG (gray dashed curve) always exceeds that of the satellites by more than an order of magnitude at  $\lambda > 2 \mu\text{m}$ , because of the larger stellar mass. The two displayed redshifts pinpoint two relevant evolutionary stages of the three smallest satellites (S2, S3, S4,  $M_* \lesssim 5 \times 10^8 M_\odot$ ):

1. *Bursty phase* ( $z \simeq 6.5$ , left panel): in this epoch the least massive satellites are all experiencing the brief ( $\lesssim 50$  Myr) burst of star formation in which they form all of their stars. At this stage they are characterized by relatively high SFRs, up to  $\text{SFR} \sim 14 M_\odot \text{yr}^{-1}$ . Hence, their stellar populations are dominated by young newly

formed stars, resulting in spectra with an intense rest-frame UV flux at  $\lambda \lesssim 2.5 \mu\text{m}$ .

2. *Passive phase* ( $z \simeq 6$ , right panel): this stage takes places  $\sim 100$  Myr later, when the star formation in the least massive satellites has been completely suppressed by SN feedback. The older stars and lack of ongoing star formation result in redder spectra. Note that at  $\lambda \lesssim 2.5 \mu\text{m}$  the flux has decreased by a factor  $\sim 10$ .

SEDs of the two most massive satellites (S5 and S6,  $M_* \gtrsim 5 \times 10^8 M_\odot$ ) are dominated by old stellar populations in both epochs, since they are older than 300 Myr. The SFH of these systems is characterized by a low-level, continuous activity fueled by merger events that produce peaks with  $\text{SFR} < 5 M_\odot \text{yr}^{-1}$  (e.g., see Figure 7 from Gelli et al. 2020). By  $z \sim 6.5$  these high-mass systems can be considered as “stabilized” since the bulk of their stellar population is already in place. As a result, their SED is almost unchanged between



the two stages. Also, in the first stage they are fainter than S2, S3, S4 due to the lower SFR, and to their more dusty nature; as lower systems fade, massive systems are the brightest ones in the passive phase.<sup>4</sup>

To highlight dust effects on the final spectra, we compare the intrinsic stellar emission for S3, S4 and S6. As the dust content broadly scales with galaxy stellar mass, massive systems suffer a larger attenuation. For instance, even though S3 and S4 have similar intrinsic fluxes at wavelengths  $\lambda \sim 1 \mu\text{m}$  during the bursty phase, the more massive S4 is more attenuated. However, low-mass systems are particularly affected by dust extinction during their starburst phase, which is characterized by higher gas column density in the star-forming regions. Interestingly, the predicted fluxes are in most cases well above the sensitivity of NIRCcam in different filters, shown for a S/N = 5 in  $\sim 3$  hr by horizontal black lines. However, these estimates are valid for point sources. To draw solid conclusions on their observability, we need to assess whether the satellites can be spatially resolved by JWST.

Figure 2 shows the synthetic images of the LBG system at  $z \sim 6$  over an area of  $2''.5 \times 2''.5$  in two wide filters (F200W and F356W). The colored pixels within the images show the flux at S/N  $\sim 3$ , with exposure times of  $\sim 20$  hr (top) and  $\sim 3$  hr (bottom). The white contours indicate<sup>5</sup> the areas with S/N  $\sim 10$ . The image shows the system at  $z \sim 6$ , i.e., the last snapshot available during the passive phase, when the three low-mass satellites are at their faintest level. This conservative choice reveals how, even in this worst case of detectability conditions during their evolution, many satellites do exceed the sensitivity threshold. Namely, the fluxes of S5 and S6 reach S/N = 10 in both filters and they are detectable in just 3 hr of observations. The emission of all five dwarf galaxy satellites exceeds the S/N = 3 sensitivity threshold in the wide filter F356W in 20 hr. In F200W, S2 and S3 remain undetected at  $z \sim 6$ , but they are detectable in  $\sim 17$  hr at previous stages when their flux is higher ( $6.5 \lesssim z \lesssim 6.2$ ). Figure 2 shows that to distinguish the dwarf galaxy satellites from the central LBG, a separation of  $\gtrsim 0''.25$  is required. Noticeably, this requirement is achieved for all dwarf satellites with the exception of S5, which is located in the inner regions (1.2 kpc from the center of Althæa) and whose emission is likely confused with that of the central LBG.

In conclusion, dwarf satellites of high- $z$  LBGs can be actually observed with JWST within the planned deep surveys exceeding  $\sim 20$  hr of exposure time. What information can be inferred from their photometry, in particular through color-magnitude diagrams (CMDs)? While retrieving colors and magnitudes, we checked the possible contamination by nebular emission lines (e.g.,  $\text{H}_\alpha$ ,  $\text{H}_\beta$ ,  $[\text{O III}]\lambda 5007$  and  $[\text{O II}]\lambda 3727$ ), post-processing the simulation outputs with CLOUDY (Ferland et al. 2017), with the caveat of not having a consistent modeling of the interstellar radiation field with radiative transfer (see Pallottini et al. 2019). Our estimates show that emission lines are expected to produce negligible variation in both color and magnitude ( $< 0.1$  dex) for the three satellites

farther from Althæa (S3, S4, S6), while the two located in its proximity ( $\lesssim 0''.4$ ) suffer heavier line contamination due to the nearby LBG disk. Figure 3 shows the CMDs from  $z \sim 6.5$  ( $t_{\text{Uni}} \sim 850$  Myr) to  $z \sim 6$  ( $t_{\text{Uni}} \sim 950$  Myr) of the three best-target satellites, which (i) are located farther from the central LBG, and (ii) can be identified in only 7 hr observations in F356W at  $z \sim 6$  (the faintest evolutionary stage).

In the upper four panels (a-b-c-d) we plot the color F200W–F356W as a function of the AB magnitude in the filter F200W, and the symbols are color-coded according to SFR, stellar metallicity,  $Z_*$ , fraction of young,  $f_*(\text{Age} < 5 \text{ Myr})$ , and metal-poor  $f_*(Z_* < 10^{-0.5} Z_\odot)$  stars. The path of each satellite in the CMD helps clarify how its SED evolves with time. We notice two trends: (i) a complex one characterizing “active” low-mass satellites (S3 and S4), which first (bursty phase) become brighter (from  $m_{AB} \approx 29$  to  $m_{AB} \approx 27$ ) with roughly constant color (F200W–F356W  $\approx -0.5$ ), and then (passive phase) become progressively dimmer and redder as they age; (ii) the simpler one of the high-mass S6, which by  $z \approx 6.5$  is already “stabilized”, i.e., old/red (F200W–F356W  $\gtrsim 0.5$ ), and therefore only shows a modest variation ( $\lesssim 1$  dex) in both magnitude and color.

Since the high-mass satellite forms only  $\sim 6\%$  of its stellar mass during the time considered, no significant variation takes place in terms of both  $Z_*$  (always super-solar, panel b) and  $f_*(Z_* < 10^{-0.5} Z_\odot)$  ( $\lesssim 15\%$ , panel d). Conversely, its SFR varies due to a short bursts of star formation (SFR  $\sim 5 M_\odot \text{ yr}^{-1}$ , panel a), which, however, is too weak to significantly affect the fraction of young stars (panel c). On the other hand, low-mass satellites, during the first  $\sim 10$  Myr displayed, experience the peak of their bursty star formation period in which they form the bulk of their stellar mass. The SFR reaches its peak ( $\gtrsim 10 M_\odot \text{ yr}^{-1}$ , panel a), and the SED is mostly determined by newly formed young ( $\gtrsim 50\%$ , panel c), and metal-poor stars ( $\gtrsim 80\%$ , panel d). The stellar metallicity shows a rapid increase during the bursty phase ( $Z_* \gtrsim 10^{-1} Z_\odot$ , panel b). Over the  $\sim 100$  Myr shown, these low-mass systems spend only  $\sim 20$  Myr in the initial bursty phase, implying that in principle, when observing a high- $z$  low-mass satellite, it will be more likely to detect it during the longer passive phase when their SFR has decreased and  $Z_*$ ,  $f_*(\text{Age} < 5 \text{ Myr})$ , and  $f_*(Z_* < 10^{-0.5} Z_\odot)$  settle to their final, constant values.

The two bottom panels (e–f) show the color F090W–F150W as a function of the F150W magnitude, and are color-coded according to the V-band dust optical depth,  $\tau_V$ , and  $N_H$ . The SED shape in this spectral range is determined by two competing factors: young stellar populations, enhancing the flux at short wavelengths, and dust drastically reducing it. The trends in the CMD show that in general more massive satellites, which are dustier and denser, have higher F090W–F150W. The smallest object displayed (S3) shows a constant trend of the F090W–F150W, reflecting its simple SFH in which it settles to constant values of metallicity and column density. More massive satellites show a more complex behavior, in which the color becomes bluer at each small burst episode. The trends of the optical depth (e) and column density (f) are associated with the color: for instance, objects with F090W–F150W  $\gtrsim 2.5$  have  $\tau_V \gtrsim 1$  and  $N_H \gtrsim 10^{22} \text{ cm}^{-2}$ .

#### 4. Discussion

Based on our high-resolution cosmological simulations, we show that JWST will be able to detect for the first time faint

<sup>4</sup> The SFR of the most massive satellite (red curve) is temporarily zero during the second stage at  $z \approx 6$  because of a recent ( $\sim 10$  Myr before) burst of star formation and the subsequent SN feedback effect.

<sup>5</sup> Flux limits for  $\sim 3$  hr are retrieved from Table 1 of <https://jwst-docs.stsci.edu/near-infrared-camera/nircam-predicted-performance/nircam-sensitivity>, which assumes circular photometric apertures 2.5 pixels in radius and  $1.2 \times$  minimum zodiacal light background. We rescale these values for 20 hr, consistently with the values reported in Rieke et al. (2019).

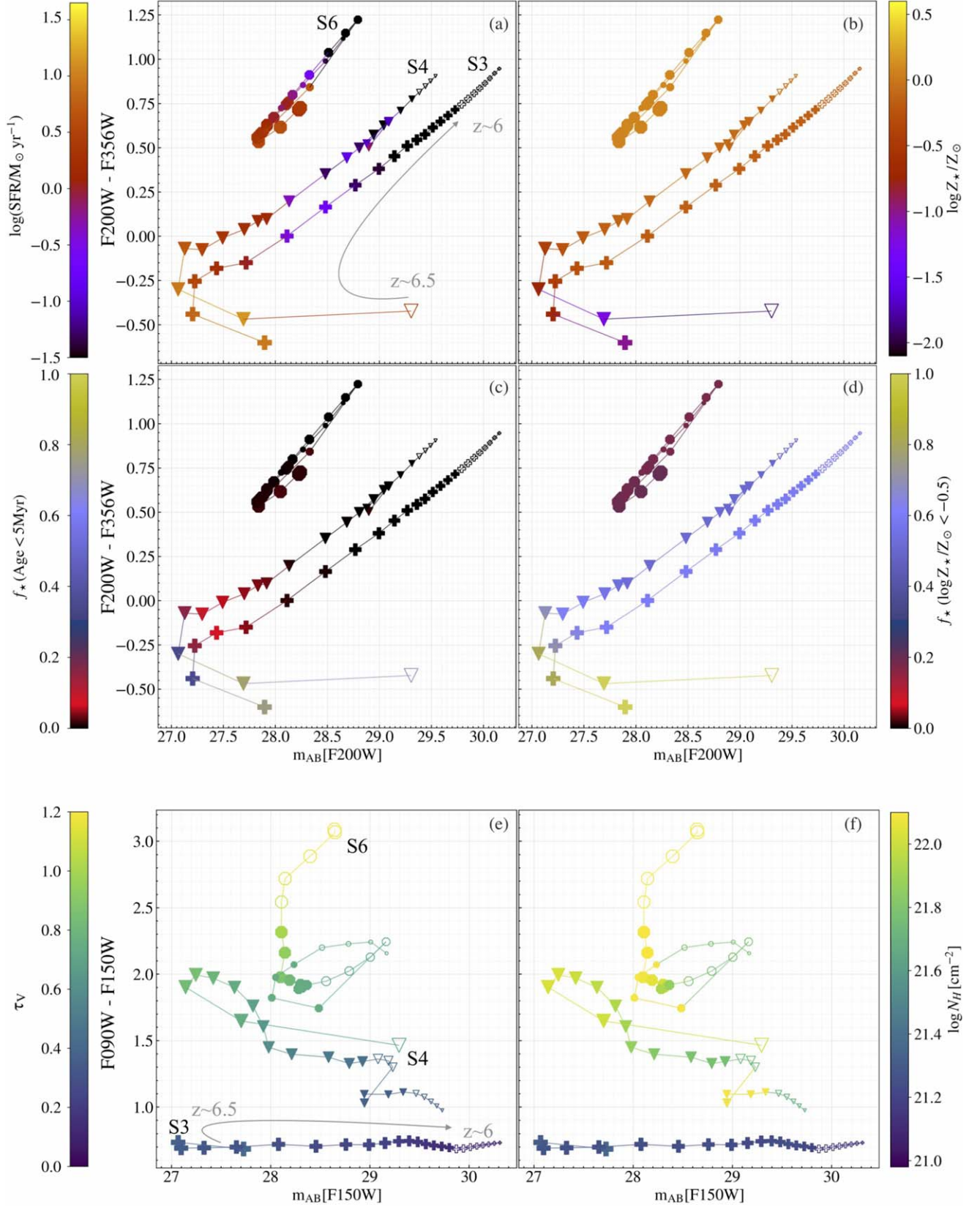


**Figure 3.** CMDs of three satellites using different NIRCcam filters. A line traces the evolution of each satellite in the diagram, the size of the markers decreasing in cosmic time from  $t \sim 850$  Myr (in correspondence of the bursty phase of low-mass satellites) to  $\sim 950$  Myr (passive phase), in steps of 5 Myr. Empty markers pinpoint the stages at which the satellite do not exceed the  $S/N = 3$  sensitivity threshold in 20 hr in the selected filters. In each panel the markers are color-coded according to different quantities. The first four characterize stellar populations: SFR, stellar metallicity, fraction of young stars (Age < 5 Myr), and fraction of metal-poor stars [ $\log Z_*/Z_\odot < -0.5$ ]. The last two refer to the ISM, i.e., the dust optical depth  $\tau_V$ , and hydrogen column density  $N_H$ .

dwarfs satellite galaxies of typical LBGs at the end of the EoR. Remarkably, this should happen already during the first planned observations. The JADES survey, for instance, will reach exposure times of  $\sim 20$  hr, sufficient for observing most satellites even during the faintest stages of their evolution. The survey will detect  $\sim 50$  LBGs with stellar mass  $M_* \sim 10^{10} M_\odot$  (Williams et al. 2018), i.e., similar to Althæa. According to our simulations, we then expect to detect a total of  $\sim 100$ – $250$  companion dwarf satellites,  $\sim 40$  of which will be most likely star bursting and dominated by young and metal-poor stars. In a future work (V. Gelli et al. 2021, in preparation) we will investigate the expected statistics of high- $z$  dwarf satellite galaxies and probability of observing them in different phases, using a larger sample of LBG targets from the SERRA suite (A. Pallottini et al. 2021, in preparation). The simulation used in this work (Pallottini et al. 2017) is ideal to study this kind of sourced as it reproduces key observed properties of known LBGs, from  $L_{[\text{C II}]}$  luminosities (Carniani et al. 2018) to the Schmidt–Kennicutt relation (Krumholz et al. 2009).






Once candidate dwarf satellites are individuated based on the proximity to a massive LBGs, a measurement of their photometric redshift is needed to infer if they do belong to the LBG system, or if we are rather dealing with an interloper. NIRCcam will be able to retrieve  $z \sim 6$  galaxies redshifts with a percentage of misidentifications as lower  $z$  galaxies of 9% (Bisigello et al. 2016), hence allowing a successful identification of the target LBG satellites.

An additional interesting finding of the simulation analysis (see Gelli et al. 2020) is the presence of a proto-globular cluster among the satellite population of the LBG at  $z \sim 6$ . This is characterized by a stellar mass  $M_* \sim 10^6 M_\odot$ , formed in an single burst of star formation ( $< 15$  Myr), and completely lacking both gas and dark matter. In this study, we find that such objects, despite their predicted existence in the vicinity of LBGs, are not bright enough to be observed with JWST/NIRCcam: more than  $\sim 1000$  hr would be required to detect their light at  $S/N \sim 3$ . Since within the JADES survey we do not expect the presence of gravitationally lensed sources, the hundreds of expected observed satellites around LBGs will be indeed dwarf galaxies, and not globular clusters (e.g., Vanzella et al. 2017). Among them, some will be most likely detected while experiencing their burst of star formation. We showed how photometric observations will be most relevant to shed the first light on high- $z$  satellite galaxies and, provided that many of these sources will be discovered in the surroundings of LBGs, we suggested that the F200W–F356W color is a powerful diagnostic tool to understand their properties. For example,

F200W–F356W  $\lesssim -0.25$  characterizes star-bursting ( $\text{SFR} \sim 5 M_\odot \text{ yr}^{-1}$ ), low-mass ( $M_* \lesssim 5 \times 10^8 M_\odot$ ), low stellar metallicity systems, with  $\sim 80\%$  of their stellar population composed by young and metal-poor [ $\log(Z_*/Z_\odot) < -0.5$ ] stars.

We thank the referee for the careful reading of the Letter and the insightful comments. We acknowledge support from PRIN-MIUR2017, prot. n.2017T4ARJ5, ERC Starting Grant NEFERTITI H2020/808240 and ERC Advanced Grant INTERSTELLAR H2020/740120.

### ORCID iDs

Viola Gelli  <https://orcid.org/0000-0001-5487-0392>  
 Stefania Salvadori  <https://orcid.org/0000-0001-7298-2478>  
 Andrea Ferrara  <https://orcid.org/0000-0002-9400-7312>  
 Andrea Pallottini  <https://orcid.org/0000-0002-7129-5761>  
 Stefano Carniani  <https://orcid.org/0000-0002-6719-380X>

### References

- Bertelli, G., Bressan, A., Chiosi, C., Fagotto, F., & Nasi, E. 1994, *A&AS*, **106**, 275
- Bisigello, L., Caputi, K. I., Colina, L., et al. 2016, *ApJS*, **227**, 19
- Carniani, S., Maiolino, R., Amorin, R., et al. 2018, *MNRAS*, **478**, 1170
- Conroy, C., Wechsler, R. H., & Kravtsov, A. V. 2006, *ApJ*, **647**, 201
- Ferland, G. J., Chatzikos, M., Guzmán, F., et al. 2017, *RMxAA*, **53**, 385
- Finkelstein, S. L. 2016, *PASA*, **33**, e037
- Gallerani, S., Maiolino, R., Juárez, Y., et al. 2010, *A&A*, **523**, A85
- Gardner, J. P., Mather, J. C., Clampin, M., et al. 2006, *SSRv*, **123**, 485
- Gelli, V., Salvadori, S., Pallottini, A., & Ferrara, A. 2020, *MNRAS*, **498**, 4134
- Grassi, T., Bovino, S., Schleicher, D. R. G., et al. 2014, *MNRAS*, **439**, 2386
- Horner, S. D., & Rieke, M. J. 2004, *Proc. SPIE*, **5487**, 628
- Jeon, M., & Bromm, V. 2019, *MNRAS*, **485**, 5939
- Kennicutt, R. C. J. 1998, *ApJ*, **498**, 541
- Kroupa, P. 2001, *MNRAS*, **322**, 231
- Krumholz, M. R., McKee, C. F., & Tumlinson, J. 2009, *ApJ*, **693**, 216
- Leitherer, C., Schaerer, D., Goldader, J. D., et al. 1999, *ApJS*, **123**, 3
- Pallottini, A., Ferrara, A., Bovino, S., et al. 2017, *MNRAS*, **471**, 4128
- Pallottini, A., Ferrara, A., Decataldo, D., et al. 2019, *MNRAS*, **487**, 1689
- Pallottini, A., Ferrara, A., Gallerani, S., Salvadori, S., & D’Odorico, V. 2014, *MNRAS*, **440**, 2498
- Rieke, M., Arribas, S., Bunker, A., et al. 2019, *BAAS*, **51**, 45
- Teyssier, R. 2002, *A&A*, **385**, 337
- Vanzella, E., Calura, F., Meneghetti, M., et al. 2017, *MNRAS*, **467**, 4304
- Weingartner, J. C., & Draine, B. T. 2001, *ApJ*, **548**, 296
- Williams, C. C., Curtis-Lake, E., Hainline, K. N., et al. 2018, *ApJS*, **236**, 33
- Wise, J. H., Abel, T., Turk, M. J., Norman, M. L., & Smith, B. D. 2012, *MNRAS*, **427**, 311
- Wise, J. H., Demchenko, V. G., Halicek, M. T., et al. 2014, *MNRAS*, **442**, 2560
- Zackrisson, E., Binggeli, C., Finlator, K., et al. 2017, *ApJ*, **836**, 78